Supporting Information

Atomically Precise Nanoclusters as SERS Probes

Sujan Manna,[a] *Anant O. Bhasin,*# [b] *Vivek Yadav,*# [a] *Soham Chowdhury,* [a] *Subrata Duary,*[a] *Sampati Mondal,*[a] *Sajal Kumar Giri,*[c] *Tomas Base,**[d] *George C. Schatz,**[e] *Thalappil Pradeep**[a][f]

[a] DST Unit of Nanoscience (DST UNS) and Thematic Unit of Excellence (TUE), Department of Chemistry, Indian Institute of Technology Madras, Chennai, 600036, India

[b] Department of Chemistry, Brandeis University, 415 South Street, Waltham, Massachusetts 02453, United States

[c] Department of Chemical Sciences, Indian Institute of Science Education and Research (IISER) Mohali, Mohali, Punjab 140306, India

[d] Department of Syntheses, Institute of Inorganic Chemistry, The Czech Academy of Sciences, Rez, 25068, Czech Republic

[e] Department of Chemical & Biological Engineering, Northwestern University, Evanston, Illinois 60208, United States

Department of Chemistry, Northwestern University, Evanston, Illinois 60208, United States

International Institute for Nanotechnology, Northwestern University, Evanston, Illinois 60208, United States

[f] International Centre for Clean Water, IIT Madras Research Park, Chennai, 600113, India

Experimental procedures:

Chemicals. Tetrachloroauric acid trihydrate ($HAuCl_4 \cdot 3H_2O$), hexadecyltrimethylammonium chloride (CTAC), sodium borohydride ($NaBH_4$), 1,2-bis(diphenylphosphino)ethane (DPPE), sodium iodide (NaI), and ascorbic acid (AA) were purchased from Sigma Aldrich. Silver nitrate ($AgNO_3$, 99.0%) was procured from Rankem, India. Ortho-carborane-1-thiol (o_1-CBT) was synthesized from an ortho-carborane precursor purchased from Katchem, Czech Republic; crystalline o_1-CBT ligands (98.9%) were used for the nanocluster synthesis. High-performance liquid chromatography (HPLC)-grade solvents, including dichloromethane (DCM, 99.8%), methanol (MeOH, 99.5%), and n-hexane (99.0%), were sourced from Rankem Chemicals and Finar, India. Milli-Q water was used for seed preparation, growth, purification, and crystallization steps. Glassware was thoroughly cleaned using aqua regia, followed by extensive rinsing with distilled water and subsequent drying under ambient conditions before use. All chemicals were commercially available and used without further purification.

Synthesis of gold nanotriangles (Au NT). Trigonal planar nanoparticles with high size and shape monodispersity were synthesized using a previously reported method.[1] The first step of the synthesis was seed preparation, where 4.7 mL of 100 mM CTAC was taken in a 20 mL glass vessel. Under mild stirring, 25 μL of 10 mM $HAuCl_4$ was mixed with it, followed by the rapid injection of 300 μL of 10 mM freshly prepared (in ice-cold water) $NaBH_4$. Vigorous stirring continued for 2 min after the addition of $NaBH_4$ to facilitate the release of hydrogen gas generated in the medium. After this, the brown-colored seed solution was kept undisturbed for 2 hours. Two separate growth solutions were then prepared.

Growth solution I, i.e., G-I. To 1.6 mL of 100 mM CTAC, 8 mL of water, 40 μL of 10 mM $HAuCl_4$, and 15 μL of 10 mM NaI were sequentially added by mild manual mixing.

Growth solution II, i.e., G-II. To 40 mL of 50 mM CTAC, 500 μL of 10 mM $HAuCl_4$ and 300 μL of 10 mM NaI were added, following the same procedure as for **G-I**. The seed solution was subsequently diluted 10 times using 100 mM CTAC. In single shots, 40 μL and 400 μL of 100 mM AA were added to **G-I** and **II**, respectively. Immediately after this, 100 μL of the diluted seed was added to **G-I** under gentle manual mixing. Within 1 s of mixing, as the color of the **G-I** turned pink, 3.2 mL of it was transferred to the **G-II**. This was mixed similarly for 10 s. Within 10 minutes, the G-II turned blue in colour.

Purification of Au NTs. As-synthesized Au NTs contained a proportion of gold nanoparticles of non-targeted shapes. To eliminate them, the flocculation method suggested by Scarabelli *et al.* was employed.[1] The synthesized Au NTs were dispersed in 175 mM CTAC by adding a suitable amount of aqueous CTAC stock solution (25 wt%) into growth solution II. The mixture was kept undisturbed for 2 hours at room temperature. As a result, Au NTs with high size and shape monodispersities were selectively precipitated, leaving the undesired particles in the supernatant. The supernatant was subsequently decanted, and the sediment was dispersed in DI water with mild sonication, yielding a greenish-blue dispersion. These purified Au NTs were centrifuged twice at 6000 rpm for 5 min and redispersed in DI water before use.

Synthesis of Ag_{17}. The Ag_{17} was synthesized at ice cold condition (≈ 0 °C) using a DPPE-assisted silver-thiolate co-reduction reaction. In brief, 20 mg $AgNO_3$ was dissolved in 5 mL of MeOH. 10 mg of o_1-CBT ligand was dissolved in 9 mL DCM, which was added under stirring conditions. After 5 minutes of the reaction, 10 mg of DPPE, dissolved in 1 mL DCM, was added to the reaction mixture. After 15 minutes of reaction, 20 mg $NaBH_4$, dissolved in 1 mL of water, was added. A brownish solution was formed, eventually converted to a dark brown solution after an overnight reaction. After 18 h of reaction, the mixture was thoroughly washed with $MeOH/H_2O$, followed by complete solvent evaporation. Then the cluster was extracted using DCM and dried on a rotavapor. The yield of the product is 78% in terms of silver. Hexagonal single crystals were grown after 10 days at 4 °C through hexane vapor diffusion into the concentrated DCM solution (20 mg mL^{-1}) of the cluster.

Immobilization of Au NTs: The immobilization of Au NTs was performed on glass substrates pretreated with (3-mercaptopropyl)trimethoxysilane (MPTMS). To maintain consistency across all experiments, the Au NT dispersions were standardized to an optical density (O.D.) of 0.5 at their localized surface plasmon resonance wavelength prior to immobilization. This normalization ensures that each batch produces substrates with comparable surface coverage, thereby minimizing variability. The resulting Au NT monolayers exhibited uniform triangular morphology and reproducibility, providing a clean and robust platform for subsequent hybridization studies.

Dropcasting of Ag_{17}: For nanohybrid formation, Ag_{17} nanoclusters were deposited onto the immobilized Au NT substrates by a controlled drop-casting procedure. A defined aliquot of freshly prepared Ag_{17} dispersion in ethanol was gently pipetted onto the NT-coated surface and allowed to spread evenly under ambient conditions. The solvent was left to evaporate slowly, ensuring uniform distribution of clusters without inducing aggregation or structural degradation. This simple, reproducible method produces well-defined hybrid substrates for SERS measurements.

Calibration: It was constructed by analyzing the relative proportions of the Ag_{17} spectral features and the CMEB internal standard, rather than relying on absolute intensities, thereby decoupling concentration-dependent variation from stochastic enhancement fluctuations. Five concentration levels (0.1, 0.5, 1.0, 2.5, and 5.0 μM) were analyzed, with 100 spectra collected per cluster across multiple mapped regions. Spectra were preprocessed by polynomial baseline subtraction and cosmic-ray removal, then averaged in groups of 20 to reduce hotspot-induced variability. It involved multivariate analysis, particularly PCA followed by PLS regression, which enabled separation of total-intensity variation from analyte-to-standard proportional changes. Averaging multiple spectra per concentration was performed to suppress local hot-spot variability and improve predictive robustness.

Data preprocessing: These steps are followed to preprocess the Raman data.

- Baseline Correction: Each raw spectrum had a polynomial (typically first- or second-order) background subtracted to remove sloping autofluorescence or detector background.
- Cosmic Ray Removal: Automated detection and removal of sharp, isolated spikes using median filtering (threshold = 3σ above local background).
- Normalization: We did not perform arbitrary intensity scaling across spectra. The plotted intensities are raw counts (after baseline subtraction).
- Statistical Analysis: Mean, standard deviation, and relative standard deviation calculated for each peak across all spatial positions.

All preprocessing was performed according to the best practices outlined by Butler et al.[2]

Enhancement Factor (EF) calculation:

SERS enhancement factors (EF) were calculated using the standard ensemble definition:

$$EF = \frac{I_{\text{SERS}}}{I_{\text{Raman}}} \cdot \frac{N_{\text{Raman}}}{N_{\text{SERS}}}$$

where $I_{\text{SERS}}$and I_{Raman} are the Raman intensities of the same vibrational mode (777 cm^{-1}) measured under identical optical conditions, and $N_{\text{Raman}}$and N_{SERS} are the number of molecules contributing to the normal Raman and SERS signals, respectively.

For Ag_{17},

The measured intensities were:

$$I_{\text{SERS}} = 1052 \text{ counts}$$

$$I_{\text{Raman}} = 101 \text{ counts}$$

Thus,

$$\frac{I_{\text{SERS}}}{I_{\text{Raman}}} = \frac{1052}{101} = 10.416$$

The number of molecules contributing to the spontaneous Raman signal was calculated from the effective confocal sampling volume:

$$N_{\text{Raman}} = A \cdot d_{\text{eff}} \cdot \rho_{\text{bulk}}$$

The diffraction-limited laser spot radius for λ = 633 nm and NA = 0.8 is:

$$r = \frac{0.61\lambda}{NA} = \frac{0.61 \times 633}{0.8} = 483 \text{ nm} = 4.83 \times 10^{-5} \text{ cm}$$

The illuminated area is therefore:

$$A = \pi r^2 = \pi(4.83 \times 10^{-5})^2 = 7.33 \times 10^{-9} \text{ cm}^2$$

For a 60× objective (NA = 0.8), the effective confocal depth was taken as 3 μm (literature value):

$$d_{\text{eff}} = 3 \times 10^{-4}\ \text{cm}$$

The bulk Raman concentration was 10 mM:

$$C = 0.01\ \text{mol L}^{-1}$$

Converted to number density:

$$\rho_{\text{bulk}} = \frac{0.01}{1000} \times 6.022 \times 10^{23} = 6.022 \times 10^{18}\ \text{molecules cm}^{-3}$$

Thus,

$$N_{\text{Raman}} = 7.33 \times 10^{-9} \times 3 \times 10^{-4} \times 6.022 \times 10^{18} = 1.33 \times 10^{7}$$

The surface density of nanoclusters per μm²:

$$1.0 \times 10^{5}\ \mu\text{m}^{-2} = 1.0 \times 10^{13}\ \text{cm}^{-2}$$

The number of clusters within the laser spot is therefore:

$$N_{\text{clusters}} = 1.0 \times 10^{13} \times 7.33 \times 10^{-9} = 7.33 \times 10^{4}$$

Each nanocluster contains 12 o1-CBT ligands. Hence,

$$N_{\text{SERS}} = 7.33 \times 10^{4} \times 12 = 8.80 \times 10^{5}$$

Substituting into the EF expression:

$$\text{EF} = 10.416 \times \frac{1.33 \times 10^{7}}{8.80 \times 10^{5}}$$

$$= 157$$

The ensemble-averaged SERS enhancement factor under these conditions is therefore:

$$\text{EF} \sim 2 \times 10^{2}$$

For Ag_{17}@Au NT,

Intensity ratio:

$$\frac{I_{\mathrm{SERS}}}{I_{\mathrm{Raman}}} = \frac{7890}{4344} = 1.816$$

Number of molecules contributing to normal Raman:

Laser spot radius:

$$r = \frac{0.61\lambda}{NA} = \frac{0.61 \times 633}{0.4} = 9.66 \times 10^{-5}\ \mathrm{cm}$$

Spot area:

$$A = \pi r^2 = 2.93 \times 10^{-8}\ \mathrm{cm}^2$$

Axial depth for NA = 0.4:

$$d_{\mathrm{eff}} \approx 8 \times 10^{-4}\ \mathrm{cm}$$

Bulk number density at 10 mM:

$$\rho_{\mathrm{bulk}} = 6.022 \times 10^{18}\ \mathrm{molecules\ cm}^{-3}$$

Thus,

$$N_{\mathrm{Raman}} = A \cdot d_{\mathrm{eff}} \cdot \rho_{\mathrm{bulk}} = 2.93 \times 10^{-8} \times 8 \times 10^{-4} \times 6.022 \times 10^{18} = 1.41 \times 10^{8}$$

Number of molecules contributing to SERS:

Particle density:

$$12\ \mathrm{particles/\mu m}^2 = 1.2 \times 10^{9}\ \mathrm{particles/cm}^2$$

Particles illuminated:

$$N_{\text{particles}} = 1.2 \times 10^{9} \times 2.93 \times 10^{-8} = 35.2$$

Area of one nanotriangle (single face):

$$A_{\text{tri}} = \frac{\sqrt{3}}{4} a^{2} = 2.245 \times 10^{-11} \text{ cm}^{2}$$

Including 90% flat orientation:

$$A_{\text{particle}} = 2.02 \times 10^{-11} \text{ cm}^{2}$$

Total metal area in laser spot:

$$S_{A} = 35.2 \times 2.02 \times 10^{-11} = 7.11 \times 10^{-10} \text{ cm}^{2}$$

For full monolayer physisorption:

$$\rho_{\text{mono}} = 1 \times 10^{14} \text{ molecules/cm}^{2}$$

$$N_{\text{SERS}} = S_{A} \cdot \rho_{\text{mono}} = 7.11 \times 10^{-10} \times 1 \times 10^{14} = 7.11 \times 10^{4}$$

Final EF:

$$EF = 1.816 \times \frac{1.41 \times 10^{8}}{7.11 \times 10^{4}}$$

$$\frac{1.41 \times 10^{8}}{7.11 \times 10^{4}} = 1984$$

$$EF = 1.816 \times 1984 = 3.6 \times 10^{3}$$

Combining these two, the overall EF= $(3.6 \times 10^{3}) \times (1.6 \times 10^{2})$= 5.76×10^{5}

So, the overall EF ~ 6×10^{5}

Now, the relative standard deviation (RSD) is calculated by the formula,

$$\mathrm{RSD}(\%) = \frac{\sigma}{\bar{x}} \times 100$$

where

- σ= standard deviation of peak intensities
- $\bar{x}$= mean intensity

Calculating the RSD from 25 locations (as shown in S8) using the above-mentioned formula, RSD = 9.1%.

Instrumentation:

Raman spectra were collected using a WiTec (now Oxford Instruments) Alpha 300 S spectrometer. Absorption spectra in solution were recorded in standard cuvettes using a PerkinElmer Lambda 365 spectrometer in the wavelength range of 200- 800 nm. Mass spectra of all the clusters were measured using the Waters Synapt G2-Si High Definition Mass spectrometer. XPS Measurements were done using an ESCA Probe TPD spectrometer of Omicron Nanotechnology. Polychromatic Al Kα was used as the X-ray source (hν = 1486.6 eV). All TEM images were collected using a JEOL 3010 high-resolution TEM operated at 200 kV. A Gatan multistage CCD camera was used to record the image. All electron microscopy samples were prepared by drop casting 10 μL of the sample onto 300-mesh Ni grids with ultrathin carbon support films. The zeta potential of Au NT was measured in the solution phase with a Malvern Zetasizer Nano ZSP.

Computational Methodology

The structure of $[\mathrm{Ag_{17}L_{12}}]^{3-}$ was taken from the crystallographic data. This structure, along with orthocarborane ligands (L) were optimized using density functional theory (DFT) with the hybrid exchange-correlation functional, B3LYP,[2–6] and the effective core potential basis set, LANL2DZ.[7] The optimization was done in the gas phase using the default convergence criteria, with self-consistent field convergence criteria of 10^{-8} au. From the electron density, the atomic charges were calculated using a Bader charge analysis[8] and the visualization was performed using the Vesta visualization package.[9] The calculation of all non-resonant Raman spectra was performed in the gas phase at the same level of theory and compared with experimental data.[10] We used the Amsterdam Density Functional (ADF) suite to perform these calculations.[11]

The UV-visible spectra of $[\mathrm{Ag_{17}L_{12}}]^{3-}$ were obtained by calculating 300 singlet excited states using Linear Response Time Dependent Density Functional Theory (LR-TDDFT) at the same level of theory (B3LYP/LANL2DZ).[12] The spectra obtained from LR-TDDFT were Lorentzian broadened by a factor of 0.12 eV. Real-time TDDFT (RT-TDDFT) was performed on $[\mathrm{Ag_{17}}]^{3-}$ at the same level of theory at its maximum absorption intensity, and the electron density evolved from the ground state density matrix.[13] All RT-TDDFT simulations utilized Gaussian pulses centered at 6 fs with a maximum peak intensity of 0.0001 au. RT-TDDFT simulations were run for 48.37 fs (2000 au) using the default convergence criteria. All LR- and RT-TDDFT simulations were performed using the NWChem software version 7.0.0.[14]

Electrodynamics simulations were performed on a gold nanotriangle (73 nm side length and 2 nm thickness) to determine its absorption, scattering, and transmittance using Finite-Difference Time-Domain (FDTD) simulations.[15,16] The nanotriangle was placed on $z = 0$ along the *xy*-plane, where the center of nanotriangle was taken to coincide with the origin. The Total Field-Scattered Field (TFSF) source was used to generate a linearly polarized plane wave with a 400-800 nm wavelength.[17,18] The simulation box was cubic, with 250 nm sides, and had perfectly matched layer (PML) boundary conditions along all sides.[19] There were two constraints on the algorithm, first, a grid size of 1 nm and second, a minimum of 50 steps per wavelength steps was utilized. Gold's dielectric function was defined using the Johnson-Christy 1972 model for the simulation.[20] Temporal resolution was chosen to be $\Delta t = 0.002$ fs for 50 ps with a shutoff condition on the intensity of the incident pulse of 0.00001, to prevent extraneous run time. Simulations were assessed using the same parameters in the absence of the gold nanotriangle. All FDTD simulations were performed using the open-source software Tidy3D.[21]

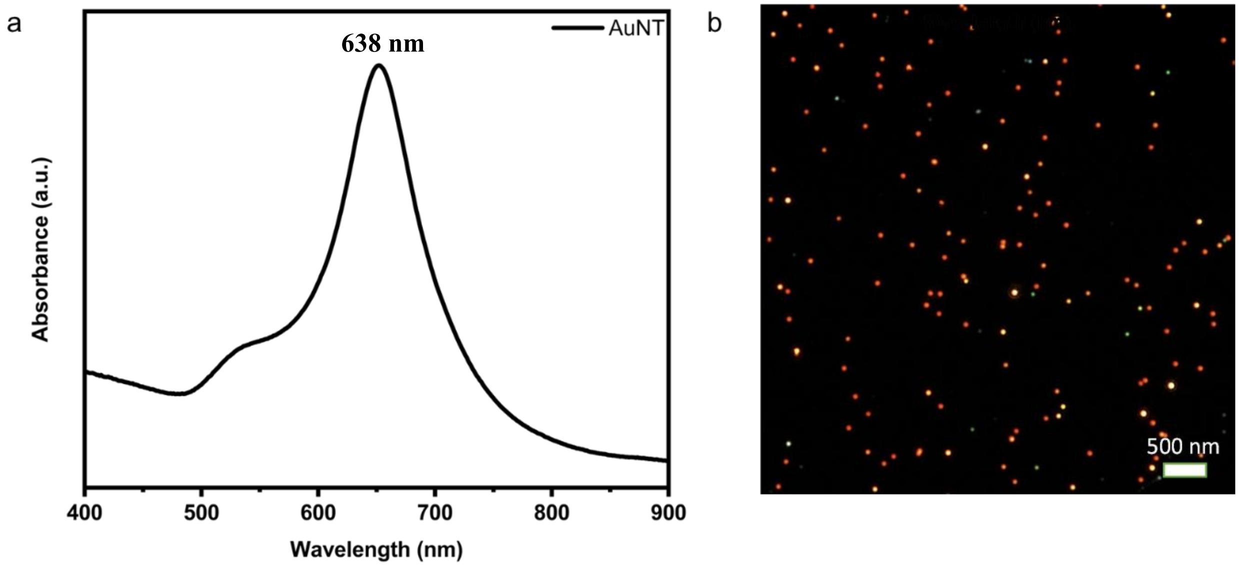

Figure S1. Characterizations of the Au NT. a) UV-vis spectrum showing the LSPR at 638 nm, b) Dark field microscopic image showing the features of the NTs.

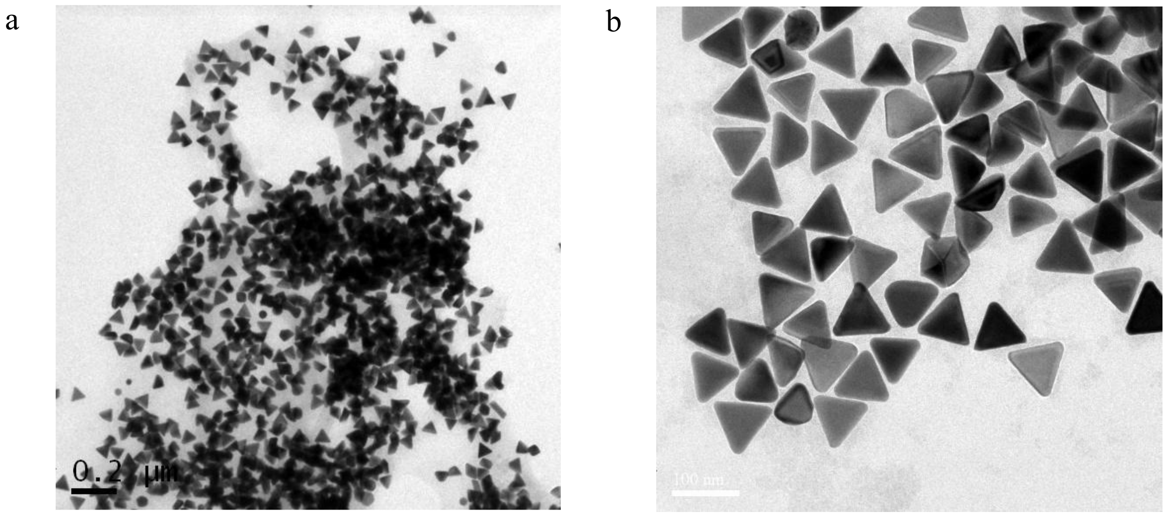

Figure S2. TEM images of Au NT. a) and b) Bulk images showing the formation of Au NTs.

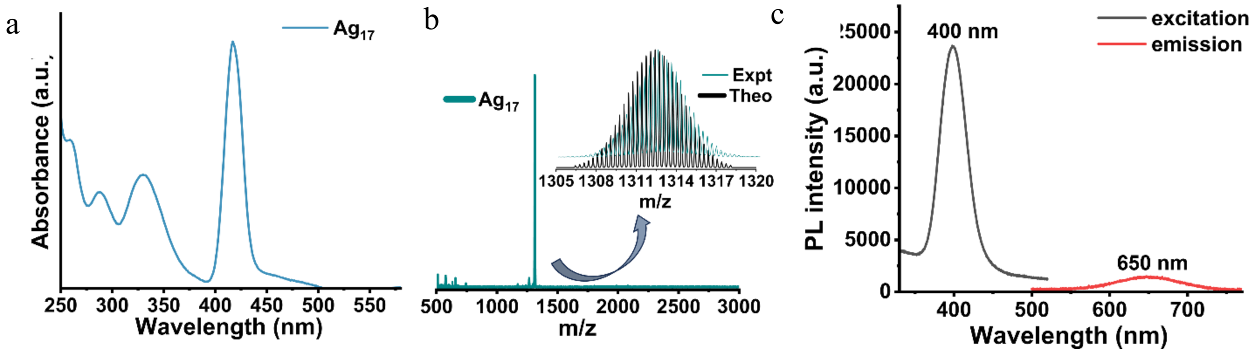

Figure S3. Characterizations of the Ag_{17} NC. a) UV-vis spectrum, b) Mass spectrum showing the major peak at m/z of 1312.42, c) PL spectrum, excitation at 400 nm and emission at 650 nm.

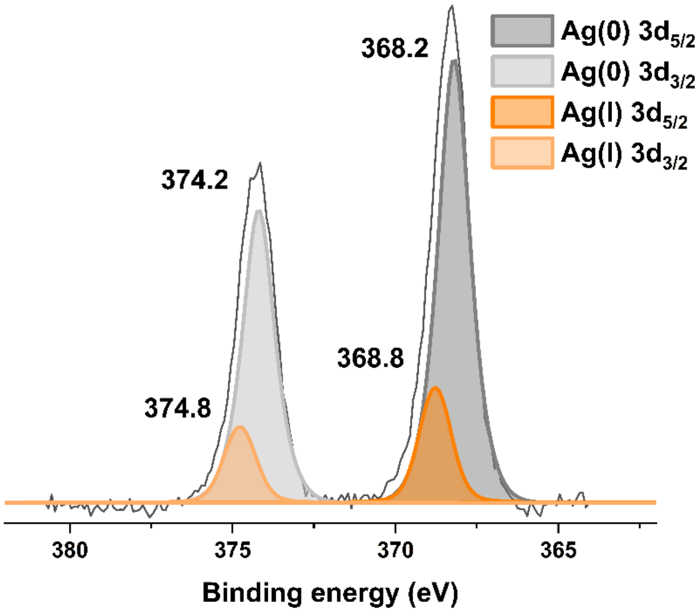

Figure S4. The XPS spectrum of raw Ag_{17} shows an Ag(0): Ag(I) ratio of 80:20.

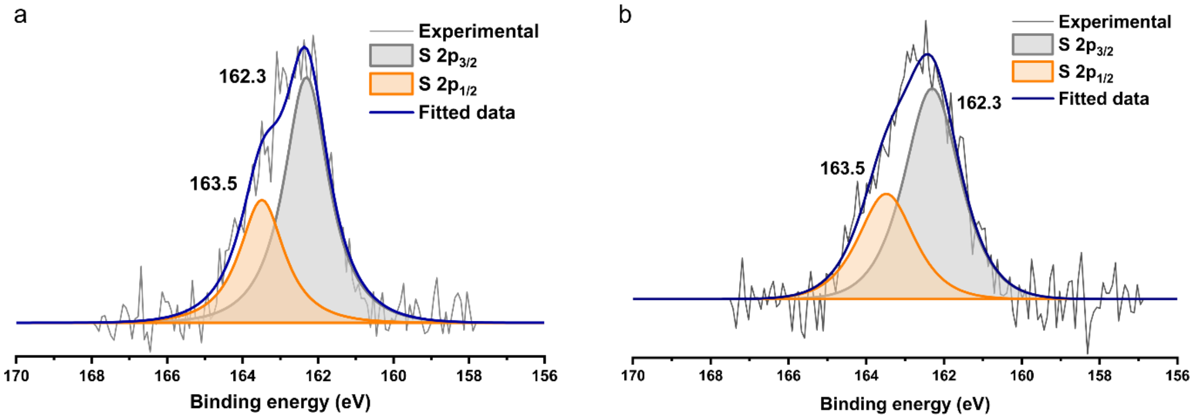

Figure S5. XPS spectra of deconvoluted Sulphur of a) Ag_{17} alone and b) Ag_{17}@ Au NT.

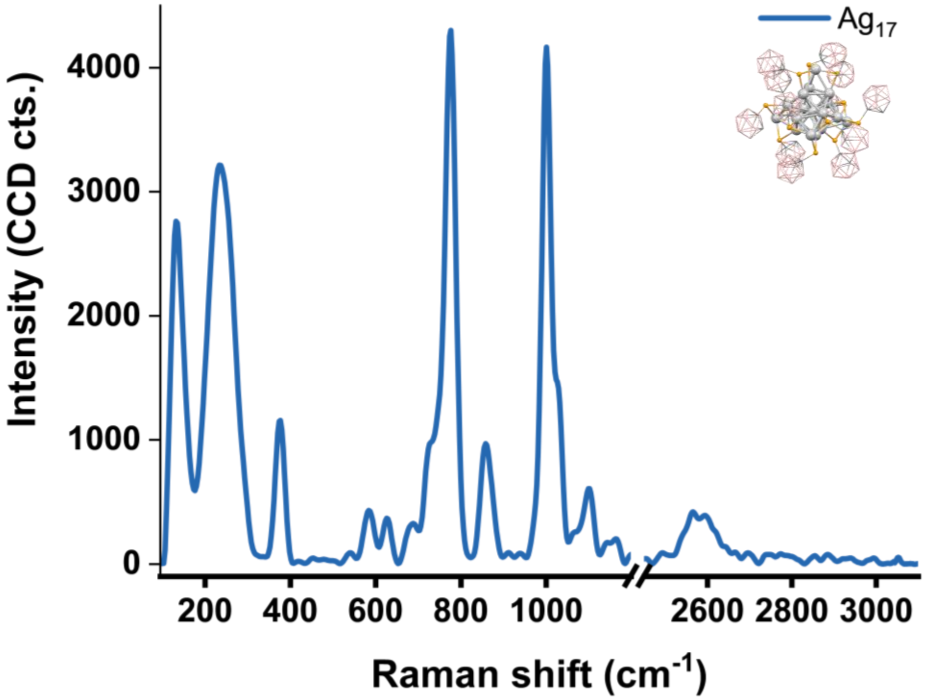

Figure S6. Raman spectrum of Ag$_{17}$.

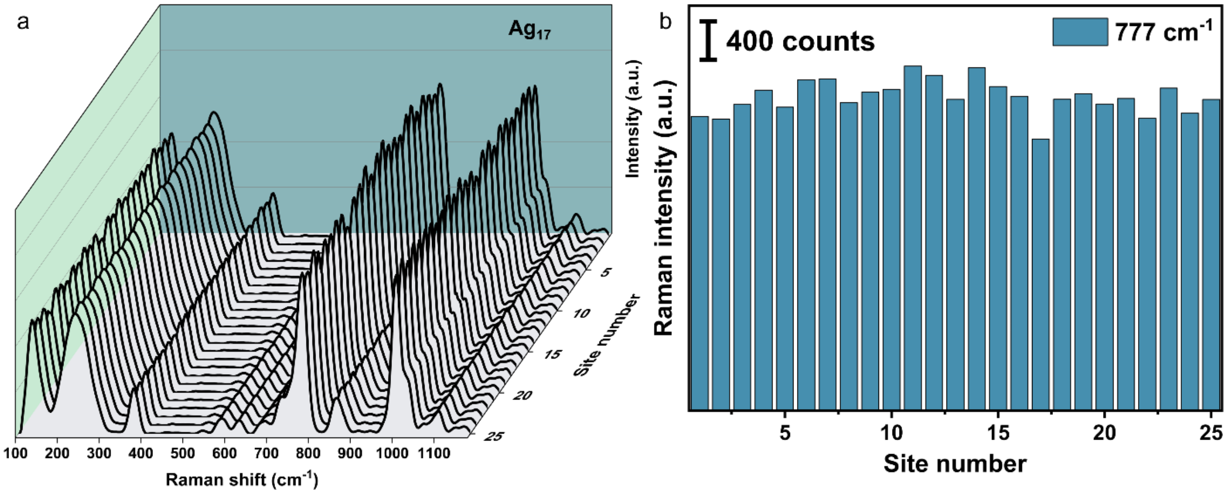

Figure S7. Reproducibility of Raman spectra of Ag$_{17}$. a) Raman spectra of Ag$_{17}$ (10 mM) collected at different positions and b) corresponding Raman peak intensity at 777 cm^{-1}. The acquisition time for each spectrum is 10 seconds with 5 accumulations.

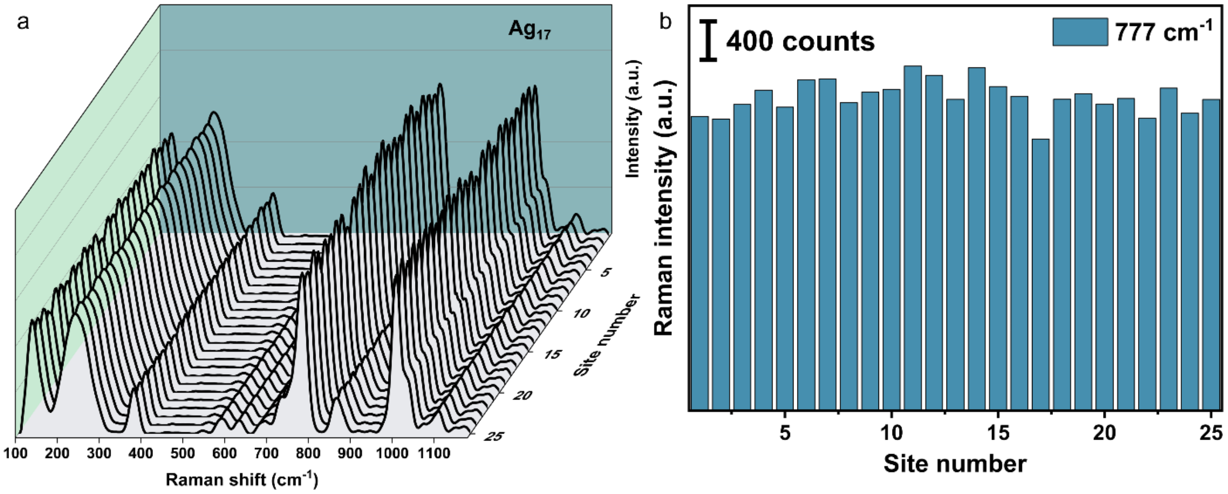

Figure S8. Reproducibility of Raman spectra of Ag_{17}@ Au NT. a) Raman spectra of Ag_{17}@ Au NT (1 μM) collected at different positions and b) corresponding Raman peak intensities at 777 cm^{-1}. The acquisition time for each spectrum is 10 seconds with 5 accumulations.

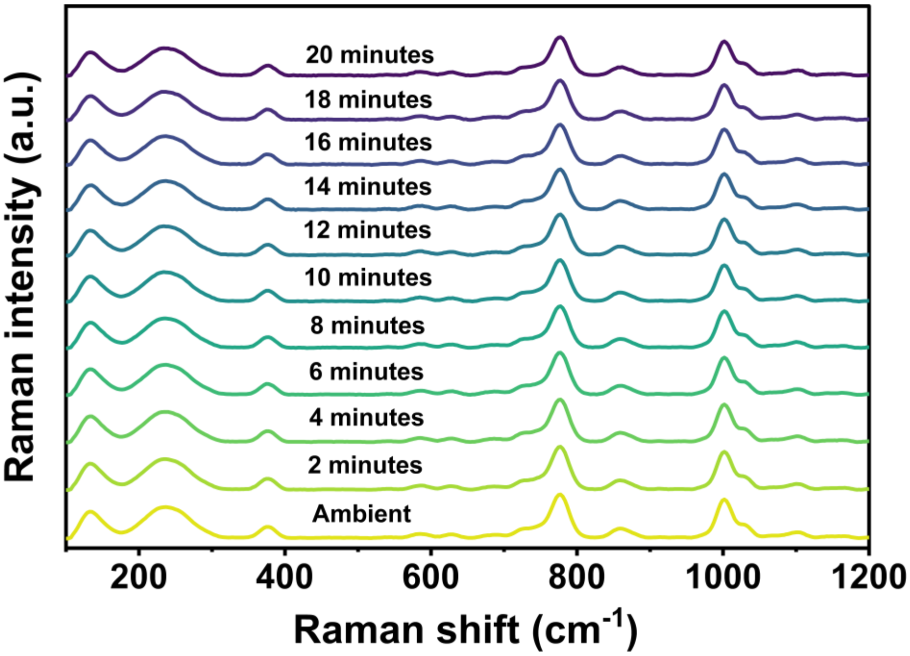

Figure S9. Photostability of Ag_{17}@Au NT under continuous laser irradiation.

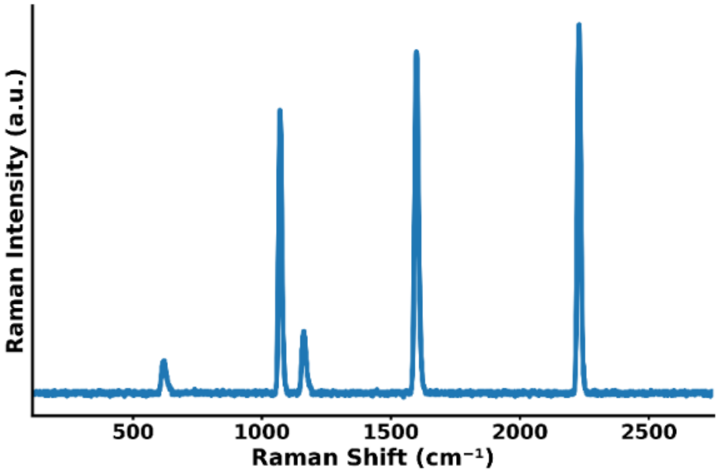

Figure S10. Surface-enhanced Raman spectrum of the CMEB.

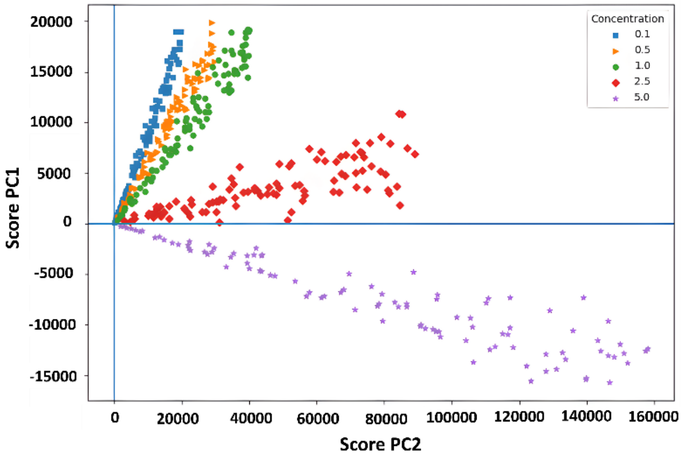

Figure S11. Plot of the PCA components 1 and 2 derived from the simulation. Average spectra were not subtracted. Each spread represents a concentration level with a simulated maximum (5% variation in the proportion between analyte and internal standard).

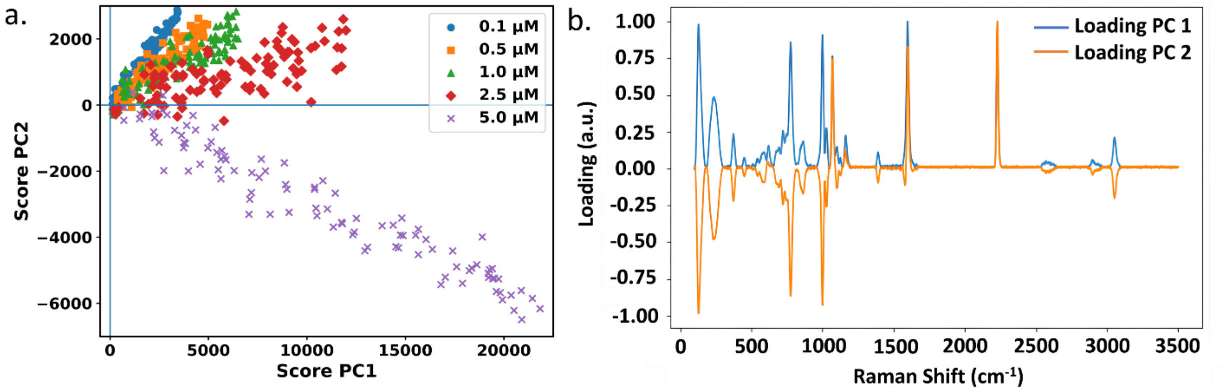

Figure S12. PCA of the original data used for the PLS model. a) A score plot with classes according to concentration. b) the corresponding loadings for the first two principal components.

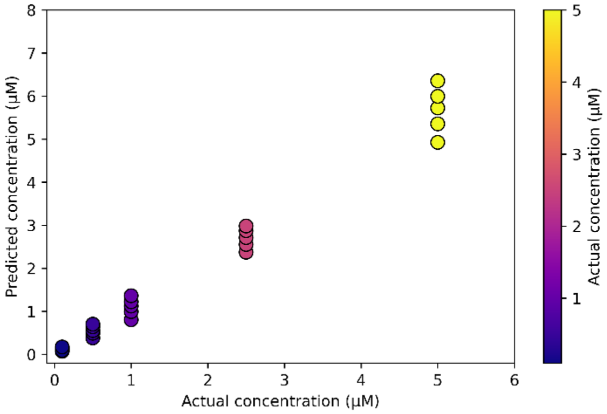

Figure S13. Actual versus predicted plot of Ag_{17} concentration in the test set used for validating the PLS model.

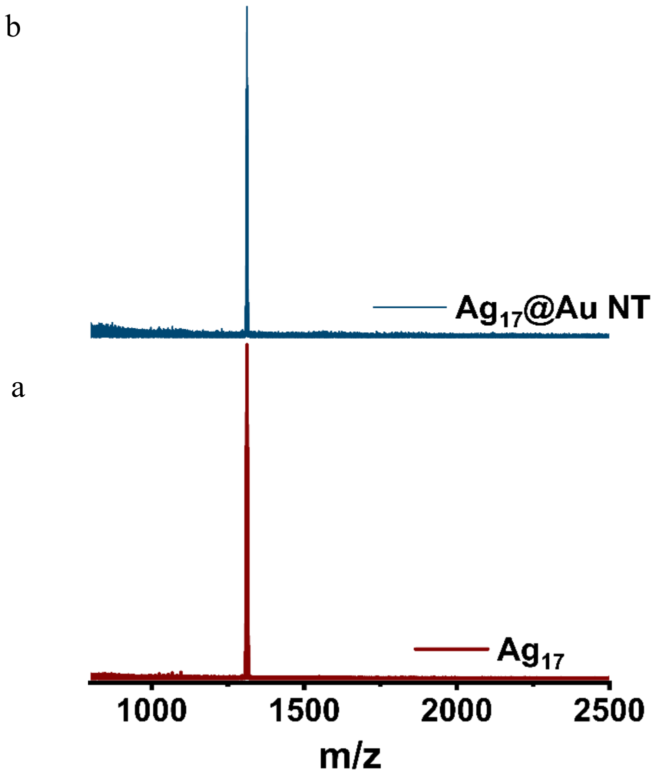

Figure S14. Comparative mass spectra of Ag$_{17}$ before and after the Au NT mixing show an unchanged mass of the Ag$_{17.}$ a) before and b) after mixing.

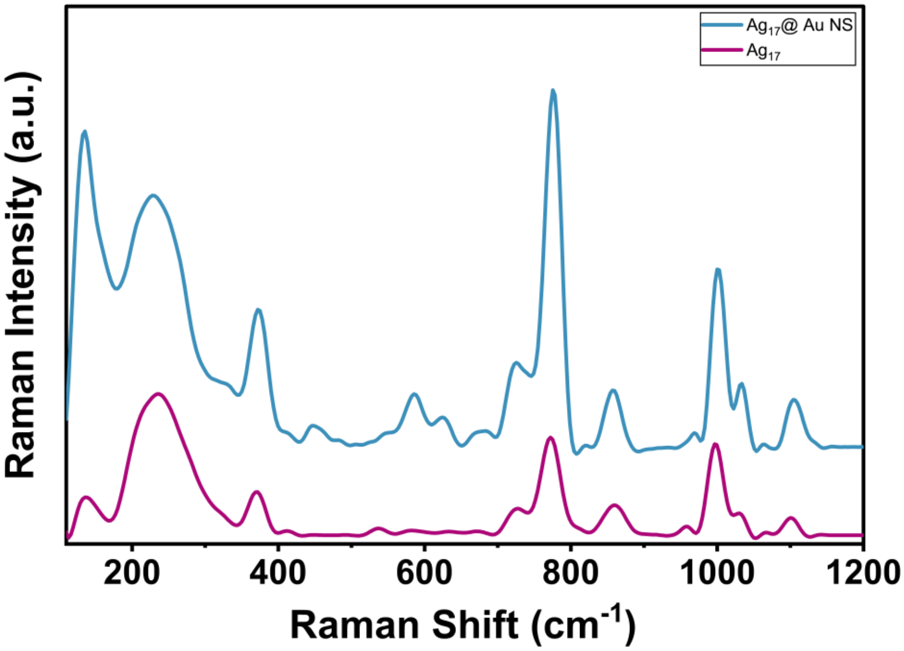

Figure S15. Raman spectra of Ag$_{17}$ vs Ag$_{17}$@ Au NS.

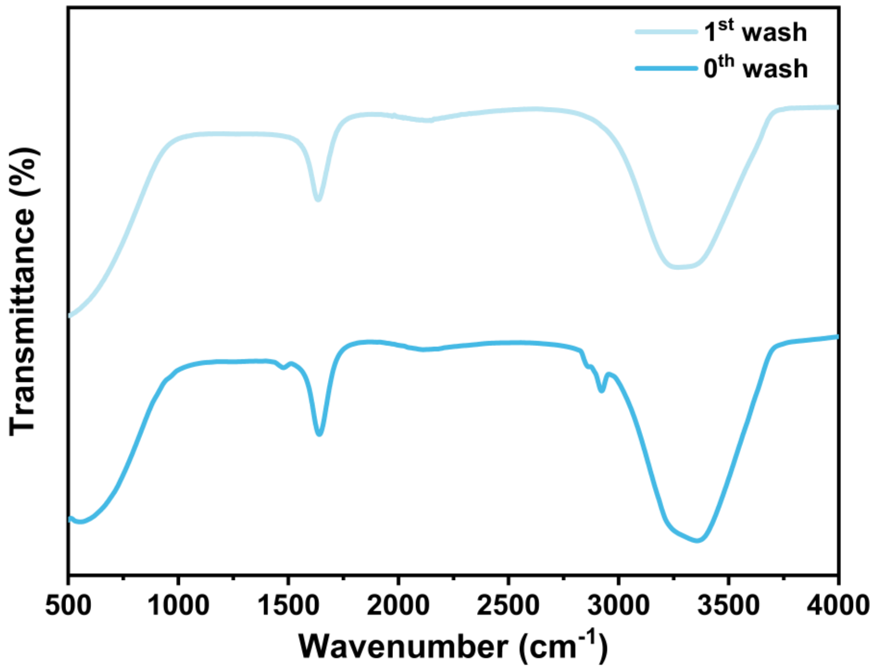

Figure S16. Comparative IR spectra of Au NT before and after washing. a) before and b) after 1st wash. It shows characteristic peaks of CTAC (peaks at 2923 and 2852 cm^{-1} due to the –CH_2 stretching of the CTAC chain, and 1467 cm^{-1} due to the deformation vibrations of –CH3 and -CH2 groups) are missing after the washing of Au NT.

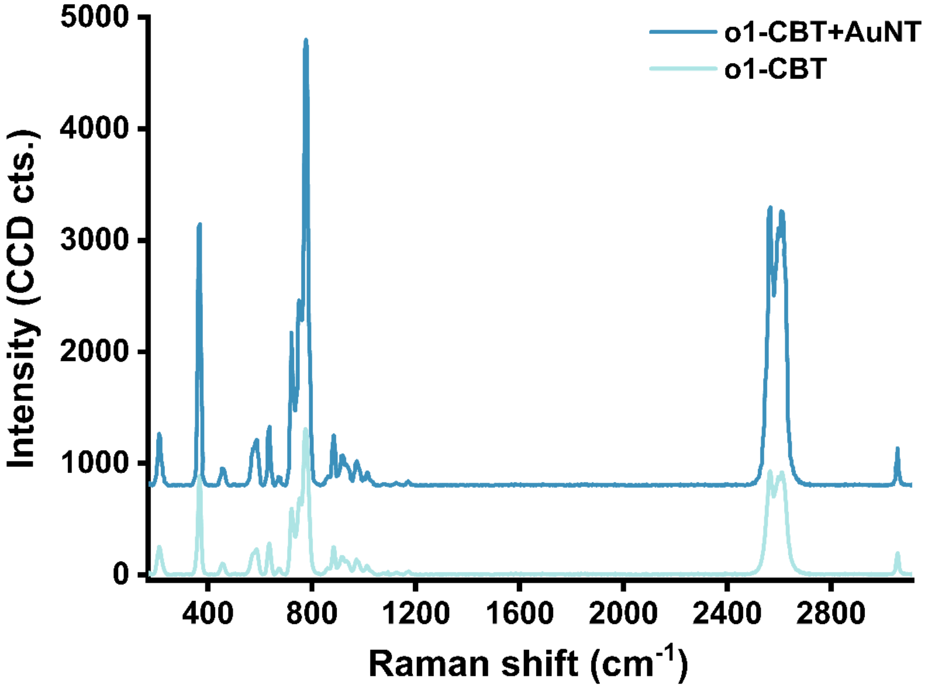

Figure S17. Comparative Raman spectra of free ligand vs Au NT+ free ligand.

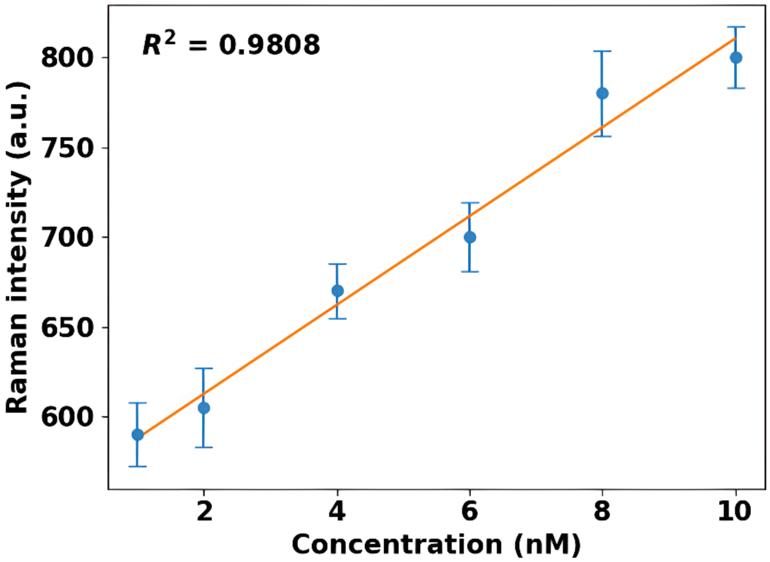

Figure S18. Calibration curve for calculating the LOD, consisting of the Raman intensity (a.u.) vs concentration (nM) for 1, 2, 4, 6, 8, and 10 nM.

From the regression earlier:

- Slope, $m = 24.726$ a.u./nM
- Residual standard deviation, $S_{y/x} = 13.498$ a.u.

Using the IUPAC definition:

$$LOD = \frac{3S_{y/x}}{m}$$

Substituting:

$$LOD = \frac{3 \times 13.498}{24.726} \text{ nM}$$

$$LOD = 1.64 \text{ nM}$$

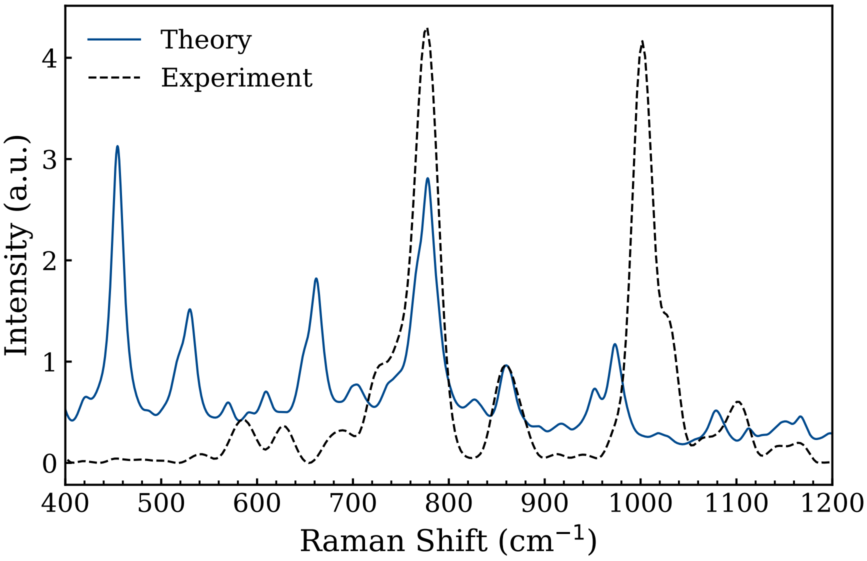

Figure S19. Comparison of experimental (--) and calculated (–) Raman spectra of $[Ag_{17}(o_1\text{-}CBT)_{12}]^{3-}$. Overall, we have gained good agreement between experimental and theoretical calculations in the region of interest.

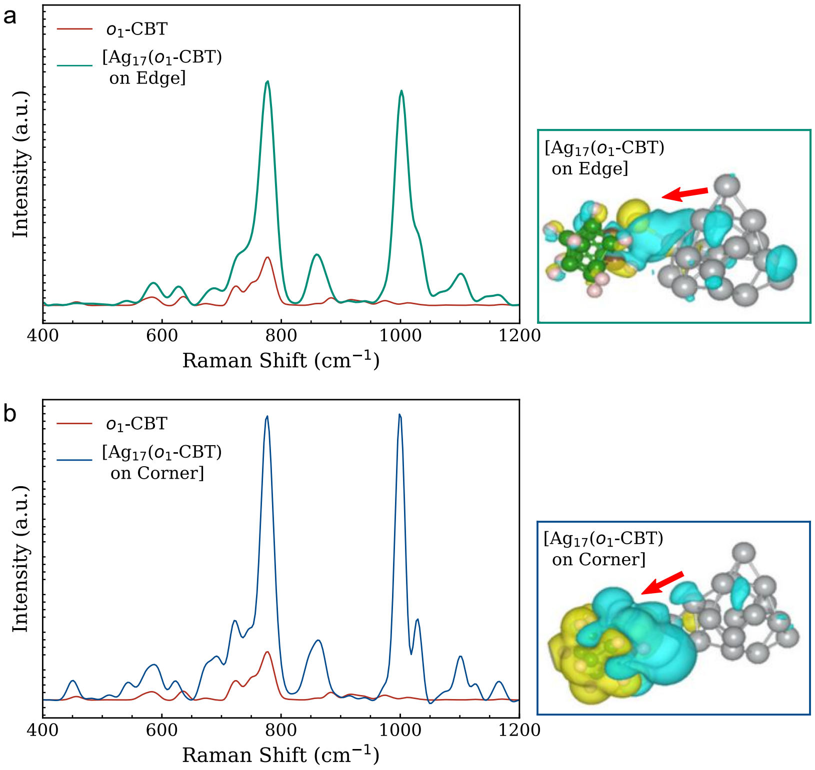

Figure S20. Raman spectra of o_1-CBT with and without Ag_{17} core in different ranges, with atomic vibrations shown at the peaks. Arrows depict the direction of charge transfer. Inset: electron density difference plots of $[Ag_{17}(o_1\text{-}CBT)]^{3-}$ with $o1 - \mathrm{CBT}$ located (a) on-edge and (b) on-corner.

Coloring of atoms: boron (green), hydrogen (white), carbon (brown), sulfur (yellow). *Iso-surface values were adjusted for visual purposes: 0.001.*

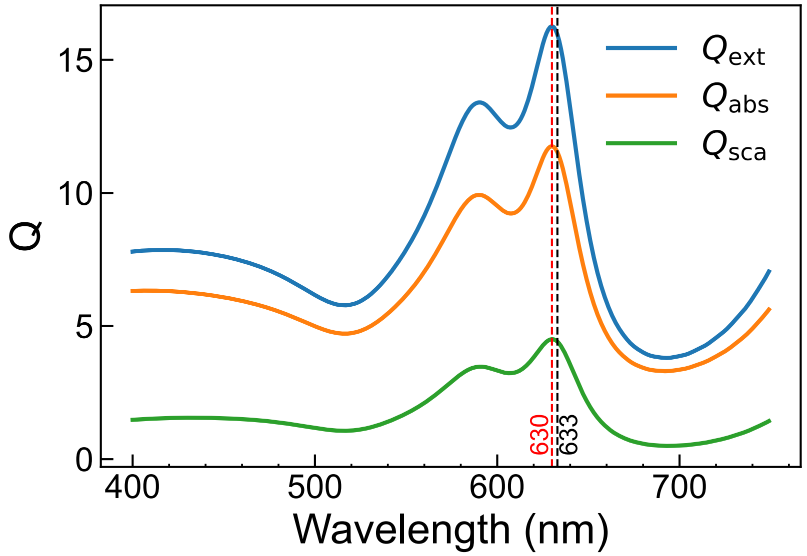

Figure S21. Simulation Results**:** Scattering, absorption, and extinction efficiency of Au NT.

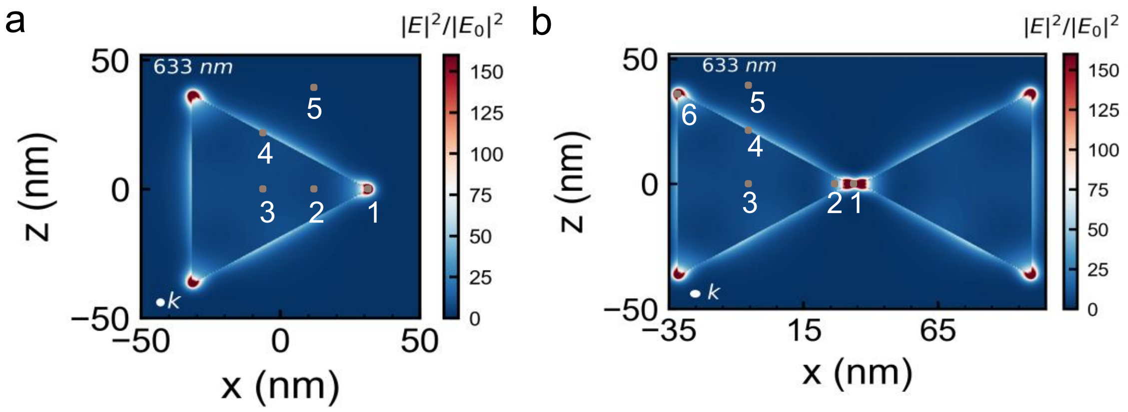

Point	**1**	**2**	**3**	**4**	**5**
Value	643.12	5.9	6.67	52.7	2.18

Point	**1**	**2**	**3**	**4**	**5**	**6**
Value	911.51	57.8	6.9	60.87	1.5	581.36

Figure S22. Simulation: Calculated electric field enhancement ($|E|^2|/E_0|^2$) from FDTD simulations for (a) single Au NT and (b) two Au NTs at 3 nm distance. In both the enhancement, value points from *1 to 4 and 6* are on the Au NT surface, and point *5* is approximately 5 nm away from the Au NT. The tables below display the distinct Enhancement factors observed at distinct locations on the surface of the NTs.

References

(1) Scarabelli, L.; Coronado-Puchau, M.; Giner-Casares, J. J.; Langer, J.; Liz-Marzán, L. M. Monodisperse Gold Nanotriangles: Size Control, Large-Scale Self-Assembly, and Performance in Surface-Enhanced Raman Scattering. *ACS Nano* **2014**, *8* (6), 5833–5842. https://doi.org/10.1021/nn500727w.

(2) Butler, H. J.; Ashton, L.; Bird, B.; Cinque, G.; Curtis, K.; Dorney, J.; Esmonde-White, K.; Fullwood, N. J.; Gardner, B.; Martin-Hirsch, P. L.; Walsh, M. J.; McAinsh, M. R.; Stone, N.; Martin, F. L. Using Raman Spectroscopy to Characterize Biological Materials. *Nat. Protoc.* **2016**, *11* (4), 664–687. https://doi.org/10.1038/nprot.2016.036.

(3) Kim, K.; Jordan, K. D. Comparison of Density Functional and MP2 Calculations on the Water Monomer and Dimer. *J Phys Chem* **1994**, *98* (40), 10089–10094. https://doi.org/10.1021/j100091a024.

(4) Stephens, P. J.; Devlin, F. J.; Chabalowski, C. F.; Frisch, M. J. Ab Initio Calculation of Vibrational Absorption and Circular Dichroism Spectra Using Density Functional Force Fields. *J Phys Chem* **1994**, *98* (45), 11623–11627. https://doi.org/10.1021/j100096a001.

(5) Lee, C.; Yang, W.; Parr, R. G. Development of the Colle-Salvetti Correlation-Energy Formula into a Functional of the Electron Density. *Phys Rev B* **1988**, *37* (2), 785–789. https://doi.org/10.1103/PhysRevB.37.785.

(6) Becke, A. D. Density-Functional Exchange-Energy Approximation with Correct Asymptotic Behavior. *Phys Rev A (Coll Park)* **1988**, *38* (6), 3098–3100. https://doi.org/10.1103/PhysRevA.38.3098.

(7) Hay, P. J.; Wadt, W. R. Ab Initio Effective Core Potentials for Molecular Calculations. Potentials for K to Au Including the Outermost Core Orbitals. *J Chem Phys* **1985**, *82* (1), 299–310. https://doi.org/10.1063/1.448975.

(8) Yu, M.; Trinkle, D. R. Accurate and Efficient Algorithm for Bader Charge Integration. *J Chem Phys* **2011**, *134* (6). https://doi.org/10.1063/1.3553716.

(9) Momma, K.; Izumi, F. VESTA 3 for Three-Dimensional Visualization of Crystal, Volumetric and Morphology Data. *J Appl Crystallogr* **2011**, *44* (6), 1272–1276. https://doi.org/10.1107/S0021889811038970.

(10) van Gisbergen, S. J. A.; Snijders, J. G.; Baerends, E. J. Application of Time-Dependent Density Functional Response Theory to Raman Scattering. *Chem Phys Lett* **1996**, *259* (5–6), 599–604. https://doi.org/10.1016/0009-2614(96)00858-5.

(11) Baerends, E. J.; Aguirre, N. F.; Austin, N. D.; Autschbach, J.; Bickelhaupt, F. M.; Bulo, R.; Cappelli, C.; van Duin, A. C. T.; Egidi, F.; Fonseca Guerra, C.; et al. The Amsterdam Modeling Suite. *J Chem Phys* **2025**, *162* (16). https://doi.org/10.1063/5.0258496.

(12) Jamorski, C.; Casida, M. E.; Salahub, D. R. Dynamic Polarizabilities and Excitation Spectra from a Molecular Implementation of Time-Dependent Density-Functional Response Theory: N2 as a Case Study. *J Chem Phys* **1996**, *104* (13), 5134–5147. https://doi.org/10.1063/1.471140.

(13) Lopata, K.; Govind, N. Modeling Fast Electron Dynamics with Real-Time Time-Dependent Density Functional Theory: Application to Small Molecules and Chromophores. *J Chem Theory Comput* **2011**, *7* (5), 1344–1355. https://doi.org/10.1021/ct200137z.

(14) Aprà, E.; Bylaska, E. J.; de Jong, W. A.; Govind, N.; Kowalski, K.; Straatsma, T. P.; Valiev, M.; van Dam, H. J. J.; Alexeev, Y.; Anchell, J.; et al. Past, Present, and Future. *J Chem Phys* **2020**, *152* (18). https://doi.org/10.1063/5.0004997.

(15) Teixeira, F. L.; Sarris, C.; Zhang, Y.; Na, D.-Y.; Berenger, J.-P.; Su, Y.; Okoniewski, M.; Chew, W. C.; Backman, V.; Simpson, J. J. Finite-Difference Time-Domain Methods. *Nature Reviews Methods Primers* **2023**, *3* (1), 75. https://doi.org/10.1038/s43586-023-00257-4.

(16) Taflove, A.; Hagness, S. C.; Piket-May, M. Computational Electromagnetics: The Finite-Difference Time-Domain Method. In *The Electrical Engineering Handbook*; Elsevier, 2005; pp 629–670. https://doi.org/10.1016/B978-012170960-0/50046-3.

(17) Merewether, D. E.; Fisher, R.; Smith, F. W. On Implementing a Numeric Huygen's Source Scheme in a Finite Difference Program to Illuminate Scattering Bodies. *IEEE Trans Nucl Sci* **1980**, *27* (6), 1829–1833. https://doi.org/10.1109/TNS.1980.4331114.

(18) Umashankar, K.; Taflove, A. A Novel Method to Analyze Electromagnetic Scattering of Complex Objects. *IEEE Trans Electromagn Compat* **1982**, *EMC-24* (4), 397–405. https://doi.org/10.1109/TEMC.1982.304054.

(19) Berenger, J.-P. A Perfectly Matched Layer for the Absorption of Electromagnetic Waves. *J Comput Phys* **1994**, *114* (2), 185–200. https://doi.org/10.1006/jcph.1994.1159.

(20) Johnson, P. B.; Christy, R. W. Optical Constants of the Noble Metals. *Phys Rev B* **1972**, *6* (12), 4370–4379. https://doi.org/10.1103/PhysRevB.6.4370.

(21) *Tidy3D, FDTD simulation solver, developed by Flexcompute Inc.*